ADVANCED FUNCTIONAL MATERIALS
www.afm-journal.de

Catalyst-Support Interactions in Zr_2ON_2-Supported IrO_x Electrocatalysts to Break the Trade-Off Relationship Between the Activity and Stability in the Acidic Oxygen Evolution Reaction

Changsoo Lee, Kihyun Shin, Youngtae Park, Young Hwa Yun, Gisu Doo, Gi Hong Jung, MinJoong Kim, Won-Chul Cho, Chang-Hee Kim, Hyuck Mo Lee, Hyun You Kim, Sechan Lee,* Graeme Henkelman,* and Hyun-Seok Cho**

The development of highly active and durable Ir-based electrocatalysts for the acidic oxygen evolution reaction (OER) is challenging because of the corrosive anodic conditions. Herein, IrO_x/Zr_2ON_2 electrocatalyst is demonstrated, employing Zr_2ON_2 as a support material, to overcome the trade-off between the activity and stability in the OER. Zr_2ON_2 is selected due to its excellent electrical conductivity and chemical stability, and the fact that it induces strong interactions with IrO_x catalysts. As a result, IrO_x/Zr_2ON_2 electrocatalysts exhibit outstanding OER performances, reaching an overpotential of 255 mV at 10 mA cm^{-2} and a mass activity of 849 mA mg_{Ir}^{-1} at 1.55 V (vs the reversible hydrogen electrode). The activity of IrO_x/Zr_2ON_2 is maintained at 10 mA cm^{-2} for 5 h, while in contrast, IrO_x/ZrN and an unsupported IrO_x catalyst undergo drastic degradation. Combined experimental X-ray analyses and theoretical interpretations reveal that the reduced oxidation state of Ir and the extended Ir—O bond distance in IrO_x/Zr_2ON_2 effectively increase the activity and stability of IrO_x by altering reaction pathway from a conventional adsorbate evolution mechanism to a lattice oxygen-participating mechanism. These results demonstrate that it is possible to effectively reduce the Ir content in OER catalysts through interface engineering without sacrificing the catalytic performance.

1. Introduction

While the global capacity of the electricity generated from renewable energy sources is forecasted to reach 4800 GW by 2026, representing a 60% increase from 2020,[1] the intermittent nature of such energy sources continues to impede their effective utilization.[2] It is currently considered that water electrolysis powered by renewable energy sources is of the most promising and practical means to overcome the limitations of intermittent renewable energy sources.[3] For example, among the various water electrolysis technologies reported to date, proton exchange membrane water electrolysis (PEMWE) possesses significant advantages, such as a high current density, system compactness, and fast response to load variations.[4] However, one of the key challenges associated with PEMWE is the development of electrocatalysts for the oxygen evolution reaction (OER), since these catalysts

C. Lee, Y. H. Yun, G. Doo, G. H. Jung, M. Kim, W.-C. Cho, C.-H. Kim, S. Lee, H.-S. Cho
Hydrogen Research Department
Korea Institute of Energy Research
152 Gajeong-ro, Yuseong-gu, Daejeon 34129, Republic of Korea
E-mail: lsc1126@kier.re.kr; hscho@kier.re.kr

K. Shin, G. Henkelman
Department of Chemistry and the Oden Institute of Computational Engineering and Sciences
University of Texas at Austin
100 E 25th Street A5300, Austin, TX 78712, USA
E-mail: henkelman@utexas.edu

K. Shin, H. Y. Kim
Department of Materials Science and Engineering
Chungnam National University
99 Daehak-ro, Yuseong-gu, Daejeon 34134, Republic of Korea
E-mail: kimhy@cnu.ac.kr

K. Shin
Department of Materials Science and Engineering
Hanbat National University
Daejeon 34158, Republic of Korea

Y. Park, H. M. Lee
Department of Materials Science and Engineering
KAIST
291 Daehak-ro, Yuseong-gu, Daejeon 34141, Republic of Korea

Y. H. Yun
Department of Chemical and Biomolecular Engineering
Yonsei University
50 Yonsei-ro, Seodaemun-gu, Seoul 03722, Republic of Korea

The ORCID identification number(s) for the author(s) of this article can be found under https://doi.org/10.1002/adfm.202301557.

DOI: 10.1002/adfm.202301557

should exhibit a high mass activity and an excellent stability in the acidic OER environment. In terms of the overall activity of water electrolysis, the OER kinetics dominate due to the fact that this process is significantly slower than the hydrogen evolution reaction (HER).[5] Although iridium oxide (IrO_2) is commonly used as an OER catalyst due to its high activity and acceptable stability,[6] the price of iridium (i.e., ≈$6000 per troy ounce) exhibited a 4-fold increase during the 2 years between 2018 and 2020,[7] thereby resulting a bottleneck for the realization of large-scale PEMWE.[8] Furthermore, IrO_2 is readily soluble in the acidic OER electrolyte, which leads to a low catalyst durability.[9]

Such limitations have driven the rational design of catalysts with high mass activities and excellent stabilities, wherein recent findings have suggested that the dispersal of IrO_x nanoparticles (NPs) on support materials with high surface areas may resolve these issues.[10] More specifically, through the homogeneous distribution of an active species over a support material, an increased electrochemically active surface area can be achieved with a reduced Ir loading. In addition, the stability and specific activity can be modulated via interfacial engineering between the Ir-based catalysts and the support materials.[11] However, conventional support materials, such as carbon-based materials or transition metal oxides, exhibit a typical trade-off relationship between their structural stability and their electronic conductivity. Although the high electronic conductivities of carbon-based support materials ensure a certain level of electrocatalytic activity even with a reduced Ir loading, they are easily corroded under a high anodic potential and in an acidic environment,[12] resulting in unavoidable decay under both constant and dynamic operations in a PEMWE. In contrast, corrosion-tolerant transition metal oxides, such as TiO_2,[13] ZrO_2,[14] Nb_2O_5,[15] MnO_2,[16] and Mn_2O_3[17] are known to exhibit poor electrical conductivities, which hinder their electrocatalytic reactions and result in the necessity for high Ir loadings.

Transition metal nitrides (TMNs) and carbides (TMCs) have therefore been suggested as support materials to overcome the above trade-off issues and achieve increased electrical conductivities and stabilities under the acidic OER environment. However, even Ti- and Zr-based nitrides[18] and carbides,[19] which are the most stable among the TMNs and TMCs, lose their excellent electron-conducting properties upon gradual oxidation and phase transformation to oxynitrides and oxides under the acidic OER environment.[20] As such, there is strong motivation to develop new support materials that can simultaneously realize a long-term stability and a sufficient electronic conductivity, which will ultimately lead to the design of high-performance, low-Ir electrocatalysts for the OER in PEMWE applications.

Thus, we herein propose Zr_2ON_2 as a novel support material for IrO_x-based OER catalysts. Zirconium oxynitride (Zr_2ON_2), which possesses a bixbyite structure with the *Ia-3* space group,[21] is selected as the support material due to the fact that it exhibits a higher thermodynamic stability than zirconium nitride (ZrN) and zirconium oxide (ZrO_2), as determined by density functional theory (DFT) calculations. In addition, the high electrical conductivity of Zr_2ON_2, which is comparable to that of graphite, lies between those of ZrN and ZrO_2,[22] and the semiconductor-like behavior of Zr_2ON_2, which has a negative temperature coefficient of resistance,[23] is beneficial for the PEMWE at a practical operational temperature of ≈80 °C.[24] In this study, Zr_2ON_2 NPs are synthesized via a sol–gel process using urea as the nitrogen source,[25] and subsequently, the oxidized Ir NPs are homogeneously dispersed on a Zr_2ON_2 support (IrO_x/Zr_2ON_2) by means of the surfactant-free polyol method,[26] followed by further electrochemical oxidation. Subsequently, the oxidation state of Ir and the Ir—O bond length in IrO_x/Zr_2ON_2 under the acidic OER conditions are determined and compared to those of unsupported catalysts using X-ray photoelectron spectroscopy (XPS) and *operando* X-ray absorption spectroscopy (XAS). Finally, based on experimental analyses and DFT calculations, we confirm the factors responsible for improving the OER catalytic activity and the stability of IrO_x supported on ZrO_2ON_2.

2. Results and Discussion

2.1. Structural Analysis

The most crucial requirements for a support material to be employed in an acidic OER environment are a good electronic conductivity, an excellent thermodynamic stability, and the ability to take part in strong interactions with the active materials. Thus, in the current study, Zr_2ON_2 NPs were employed as support materials for Ir-based electrocatalysts, and their performances were compared with those of other Zr-based materials. The Zr_2ON_2 NPs were prepared via a previously reported urea–glass route,[25] which is a synthetic process based on the sol–gel technique. In addition, ZrN and ZrO_2 NPs were synthesized as alternative support materials under different heat-treatment conditions for comparison. The transmission electron microscopy (TEM) and high-resolution TEM (HRTEM) images presented in Figure S1a,b (Supporting Information) indicate the successful synthesis of the Zr_2ON_2 NPs, which are observed as homogeneously distributed nanosized particles. In the HRTEM images, the lattice fringes with spacings of 0.415, 0.292, and 0.186 nm corresponded to the (220), (222), and (521) planes of Zr_2ON_2, respectively. In addition, the particle size distribution of the Zr_2ON_2 NPs predicted an average diameter of 15.95 nm (Figure S2a, Supporting Information). The successful syntheses of the ZrN and ZrO_2 NP support materials were also confirmed by TEM and X-ray diffraction (XRD) analyses, as depicted in Figures S3 and S4 (Supporting Information). It was found that the synthesized ZrO_2 NPs possessed an average particle size of 18.42 nm, while the ZrN NPs were significantly larger (i.e., >100 nm) due to the longer heat-treatment time employed.

Following preparation of the support materials, a surfactant-free polyol method[26] was employed to obtain the supported Ir catalyst (denoted by IrO_x/Zr_2ON_2) with different Ir loading

W.-C. Cho
Department of Future Energy Convergence
Seoul National University of Science and Technology
232 Gongneung-ro, Seoul 01811, Republic of Korea
C.-H. Kim
School of Energy Technology / Hydrogen Energy
Korea Institute of Energy Technology
21 KENTECH-gil, Naju 58330, Republic of Korea

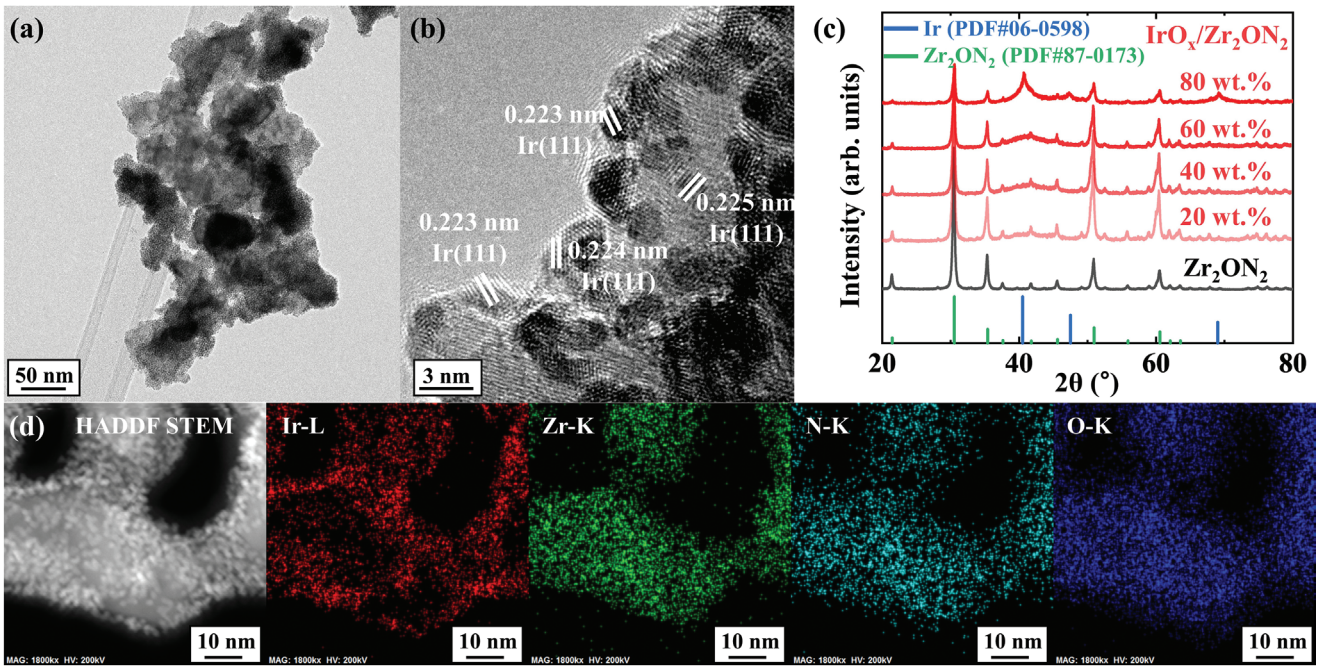

Figure 1. Physical characterization of IrO_x/Zr_2ON_2. a) TEM image and b) HRTEM image of IrO_x/Zr_2ON_2; c) XRD spectra of IrO_x/Zr_2ON_2 with varying Ir loadings and Zr_2ON_2 (PDF Nos. 06–0598 and 87–0173 for Ir and Zr_2ON_2, respectively); and d) HADDF-STEM image and EDS elemental mapping images of IrO_x/Zr_2ON_2.

amounts (i.e., 20, 40, and 60 wt.%). As shown in **Figure 1**a, the Ir NPs were well dispersed on the Zr_2ON_2 surface without agglomeration. A lattice spacing of 0.223–0.225 nm, which was assigned to the (111) plane of metallic Ir, can be seen in Figure 1b, further verifying the existence of Ir NPs. In addition, the broad XRD peak centered at 41° (Figure 1c) indicates the presence of nanosized Ir in IrO_x/Zr_2ON_2. To establish the presence and crystalline phase of supported Ir NPs, we performed XRD analysis on IrO_x/Zr_2ON_2 electrocatalysts with varying Ir loadings (20–80 wt.%). Our results indicate that IrO_x/Zr_2ON_2 with higher Ir content exhibit more prominent peaks corresponding to metallic Ir in a face centered cubic (FCC) phase. The average particle size of the Ir NPs in IrO_x/Zr_2ON_2 was determined to be 2.11 nm, as shown in Figure S2b (Supporting Information). Furthermore, the summarized energy dispersive X-ray spectroscopy (EDS) results presented in Table S1 (Supporting Information) demonstrate that the final Ir loadings matched well with the precursor ratios. Moreover, the high-angle annular dark-field scanning transmission electron microscopy (HAADF-STEM) image and the corresponding EDS elemental mapping images confirm that the Ir NPs were spatially separated from Zr_2ON_2, being predominantly located at the surfaces of the Zr_2ON_2 NPs (Figure 1d).

Control catalysts were also prepared for comparison using ZrN (IrO_x/ZrN) or ZrO_2 (IrO_x/ZrO_2) as the support material to evaluate the influence of the Zr-based support material on the properties of the resulting catalyst. Importantly, Zr_2ON_2 was found to possess an excellent electrical conductivity of ≈10–10^4 S cm^{-1}, which is comparable to that of graphite (≈10^4 and ≈10^2 S cm^{-1} for the a- and c-axes, respectively), and falls between those of ZrN (10^4–10^5 S cm^{-1}) and ZrO_2 (10^{-12}–10^{-7} S cm^{-1}). In addition, Zr_2ON_2 was found to be thermodynamically more stable than the other catalysts. The DFT-calculated formation energies of Zr_2ON_2 (–3.51 eV), ZrN (–1.51 eV), and ZrO_2 (–2.31 eV) confirmed the structural robustness of Zr_2ON_2. Moreover, as mentioned above, the TEM images (Figure 1a,b) suggest that the Ir NPs are well distributed on the Zr_2ON_2 surface without agglomeration, and this is naturally driven by the strong interactions between IrO_x and Zr_2ON_2. Overall, these results suggest that the use of Zr_2ON_2 as a support may positively affect the OER performance of the IrO_x catalyst.

2.2. Electrocatalytic OER Performance

All catalyst samples were electrochemically oxidized by repeated CV cycles (5 cycles) in the potential range of 0–1.5 V (vs RHE for all potentials) at a scan rate of 20 mV s^{-1} prior to evaluating their OER activities. Initially, the polarization curves and mass activities of IrO_x/Zr_2ON_2 with different Ir loadings (i.e., 20, 40, 60, and 80 wt.%) were compared. As shown in Figure S5a–c (Supporting Information), IrO_x/Zr_2ON_2 with an Ir loading of 40 wt.% exhibited the highest mass activity of 849 mA mg_{Ir}^{-1} at 1.55 V, although the OER overpotential of 255 mV was reduced to 248 mV upon increasing the catalyst loading to 60 wt.%. Based on this result, the initial Ir loading was fixed at 40 wt.% for all subsequent experiments.

Of the prepared IrO_x/Zr_2ON_2, IrO_x/ZrN, and IrO_x/ZrO_2 catalysts, it was found that IrO_x/Zr_2ON_2 exhibited the highest catalytic activity, which was comparable to that of commercial IrO_x-based electrocatalysts (**Figure 2**a). More specifically, the overpotentials at a geometric current density of 10 mA cm^{-2} were determined to be 255, 283, and 290 mV for IrO_x/Zr_2ON_2, IrO_x/ZrN, and IrO_x/ZrO_2, respectively. In addition, the Tafel plots

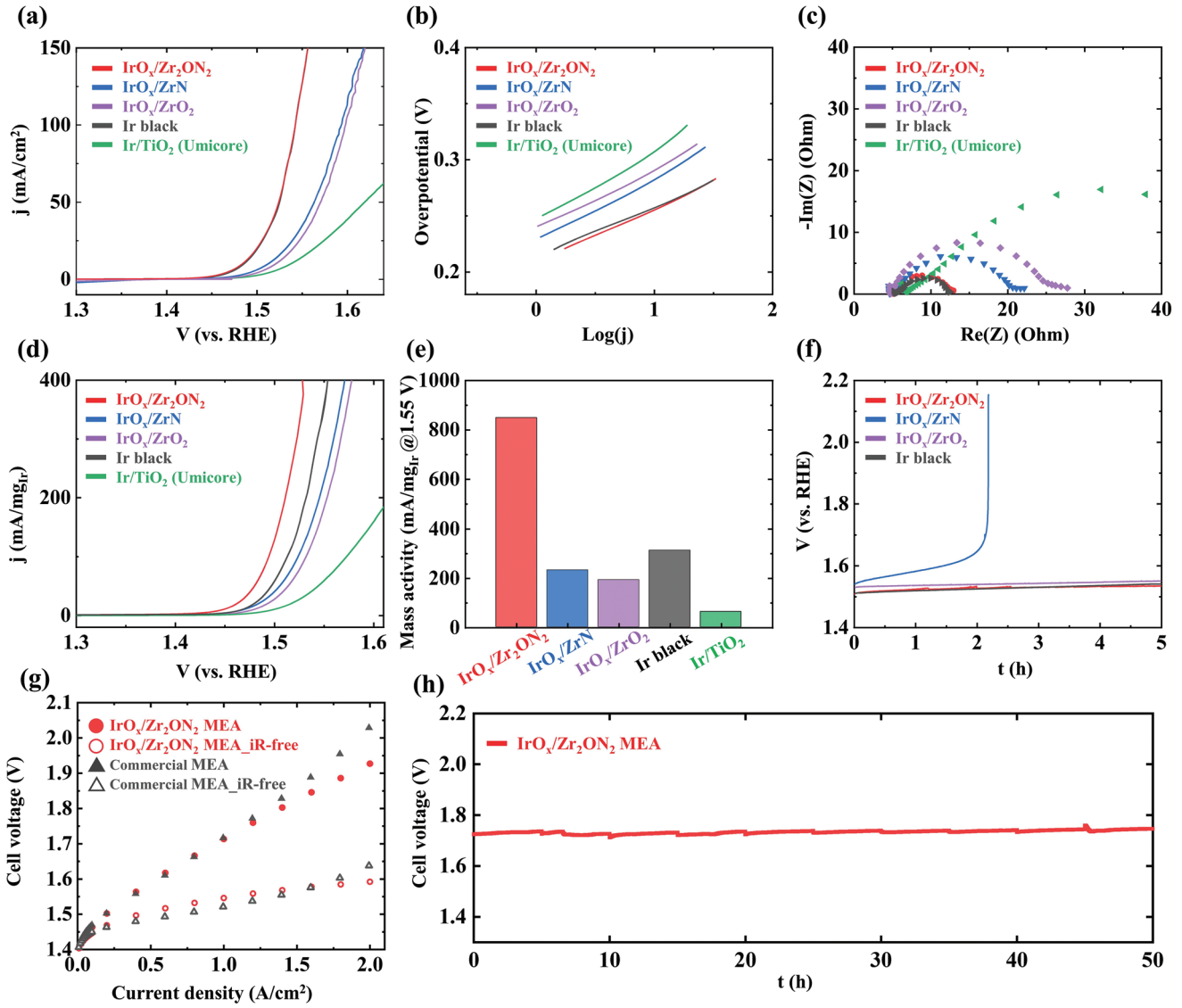

Figure 2. Electrochemical OER performances of IrO_x/Zr_2ON_2, IrO_x/ZrN, and IrO_x/ZrO_2 compared to those of the commercial Ir black and IrO_x/TiO_2 (Umicore). a) OER polarization curves; b) Tafel plots; c) electrochemical impedance spectroscopy at 1.53 V (vs RHE); d) Ir mass-normalized OER polarization curves; e) mass activities at 1.55 V (vs RHE); and f) chronopotentiometry curves recorded over 5 h at 10 mA cm^{-2}. All electrochemical measurements were conducted in an Ar-saturated 0.5 M H_2SO_4 solution; g) Single cell *I–V* curves of fabricated MEA with IrO_x/Zr_2ON_2 and commercial MEA; h) Single cell stability test at 1.0 A cm^{-2} in 80 °C; Active area for the fabricated MEA is 9 cm^2. Ir loading amounts for the fabricated MEA with IrO_x/Zr_2ON_2 and commercial MEA are 0.4 and 2.0 mg_{Ir} cm^{-2}, respectively.

(Figure 2b) confirmed that the fastest OER kinetics occurred in IrO_x/Zr_2ON_2 (48.0 mV dec^{-1} Tafel slope), while the Nyquist plots predicted that the lowest resistance existed in IrO_x/Zr_2ON_2. As a result, IrO_x/Zr_2ON_2 exhibited the highest mass activity (i.e., mass-normalized current density) of 849 mA mg_{Ir}^{-1} at 1.55 V, which is ≈3- and 14-times higher than those of the commercial IrO_x and IrO_x/TiO_2 electrocatalysts, respectively (see Figure 2d,e). The electrochemical performances of all the samples are summarized in Table S2 (Supporting Information), including data on overpotentials, mass activities, Tafel slopes, and charge transfer resistances. To the best of our knowledge, IrO_x/Zr_2ON_2 outperforms previously reported Ir-based OER catalysts in terms of the overpotential and mass activity (Table S3, Supporting Information). Subsequently, the durabilities of the three catalysts were examined under OER conditions using chronopotentiometry measurements performed at 10 mA cm^{-2} for 5 h (Figure 2f). Although the IrO_x/Zr_2ON_2, IrO_x/ZrO_2, and IrO_x catalysts exhibited marginal changes in their measured potentials during continuous OER operation, ultimately demonstrating their outstanding electrochemical robustness, it should be noted that the IrO_x/ZrN catalyst underwent severe degradation within 2 h, indicating its chemical instability in the acidic OER environment. In addition, the morphology of IrO_x/Zr_2ON_2 after a 5 h half-cell stability test was characterized using TEM analysis and EDS elemental maps. As illustrated in Figure S6 (Supporting Information), the IrO_x NPs remained

well dispersed on Zr_2ON_2 support material, demonstrating the robustness of IrO_x/Zr_2ON_2 electrocatalysts.

To further verify the feasibility of IrO_x/Zr_2ON_2 electrocatalysts as an anode for PEMWE, we evaluated single cell performances through *I–V* curve measurement and a long-term stability test at 1.0 A cm^{-2} for 50 h. As depicted in Figure 2g, the fabricated membrane electrode assembly (MEA) with IrO_x/Zr_2ON_2 exhibited a cell voltage of 1.927 V at 2.0 A cm^{-2}, which was even lower than that of a commercial MEA. Notably, the Ir loading amount in the fabricated MEA with IrO_x/Zr_2ON_2 was 0.4 mg_{Ir} cm^{-2}, while that of the commercial MEA was 2.0 mg_{Ir} cm^{-2}. Additionally, the single cell performance of the fabricated MEA with IrO_x/Zr_2ON_2 remained stable over 50 h with a negligible potential increase, as shown in Figure 2h. The results of the single cell tests clearly confirm the feasibility and robustness of IrO_x/Zr_2ON_2 as a practical anode electrocatalysts for PEMWE.

2.3. XPS and Operando XAS Analyses

To rationalize the superior OER activity and stability of IrO_x/Zr_2ON_2, XPS and X-ray absorption spectroscopy (XAS) were used to monitor the oxidation state of Ir. As shown in **Figure 3**a, the Ir 4*f* XPS spectra were deconvoluted into five spin-orbit coupled peaks.[27] The split coupled peaks at 60.8 and 63.9 eV (blue color) correspond to Ir^0 $4f_{7/2}$ and Ir^0 $4f_{5/2}$, respectively, while those at 61.6 and 64.7 eV (red color) were attributed to Ir^{4+} $4f_{7/2}$ and Ir^{4+} $4f_{5/2}$, respectively.[27,28] In addition, the peaks at 62.4 and 65.5 eV (green color) were assigned to Ir^{3+} $4f_{7/2}$ and Ir^{3+} $4f_{5/2}$, respectively,[27,28] and all other split peaks close to 62.7, 65.8, 63.4, and 66.8 eV were attributed to satellite peaks of the Ir^{3+} and Ir^{4+} states.[27,28] Quantitative analysis was performed on the deconvoluted Ir 4*f* peaks of IrO_x/Zr_2ON_2 and commercial IrO_x, both before and after the preliminary electrochemical oxidation. The as-prepared IrO_x/Zr_2ON_2 shows Ir $4f_{7/2}$ peak closed to the binding energy of Ir^0, as depicted in Figure S7a,b (Supporting Information) This peak shifted to a higher binding energy after the preliminary electrochemical oxidation of Ir through the repeated CV. As shown in Figure 3b, IrO_x/Zr_2ON_2 possesses a lower Ir^{3+} content and a higher Ir° content compared to the commercial IrO_x, indicating that the Ir component of IrO_x/Zr_2ON_2 possesses reduced chemical oxidation states. Generally, a higher Ir^{3+} content is beneficial to the OER activity, despite the fact that it is prone to degradation.[11b,29] In this context, She et al. summarized recent research related to the stability issues of Ir-based OER electrocatalysts, suggesting that the dissolution of Ir occurs in the form of Ir^{3+} and $Ir^{>4+}$.[6] In addition, Cherevko et al. suggested the formation of an Ir^{3+} intermediate to be the origin of the lower stability of both metallic and hydrous iridium oxide catalysts.[30] Furthermore, according to the degradation mechanism proposed by Kasian et al., the dissolution of Ir^{3+} is kinetically faster than the further oxidation of IrO_2 in the case of highly active electrocatalysts.[31] Figure S8a–c (Supporting Information) indicated the Ir 4*f* XPS spectra, their quantitative analysis, and the quantitative ratio of Ir^{3+}/Ir^{4+}after the 5 h stability test for the IrO_x/Zr_2ON_2 and commercial IrO_x, respectively. Despite the long-term operation causing a further oxidation from the initial activation process, consuming the Ir^0, IrO_x/Zr_2ON_2 still remained the lower ratio

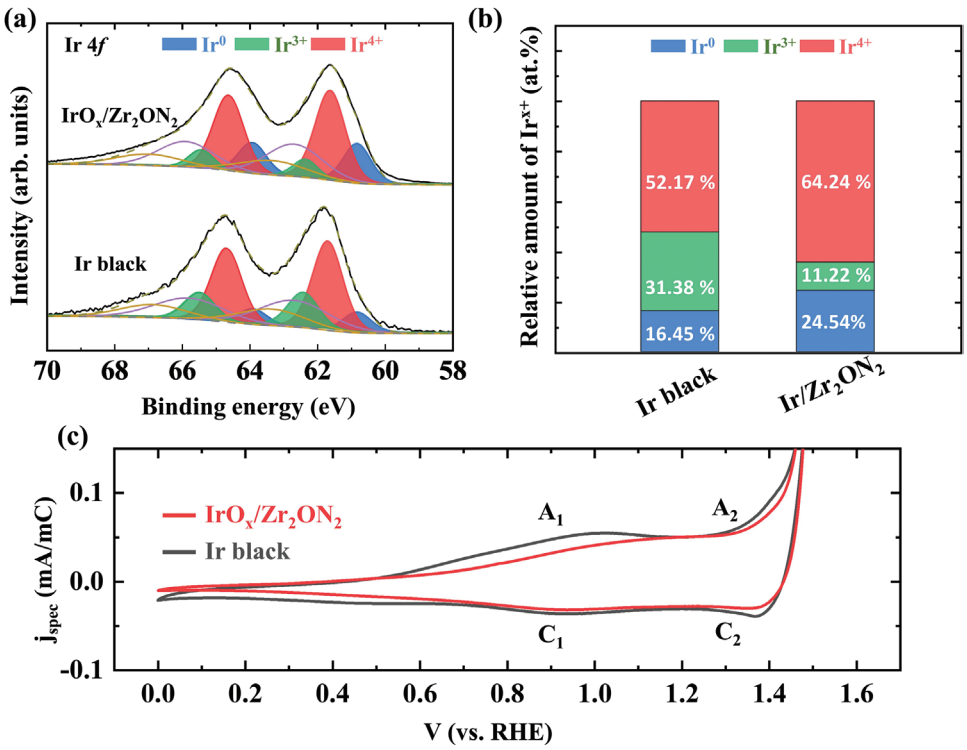

Figure 3. Chemical states of Ir in IrO_x/Zr_2ON_2 and Ir black. a) Ir 4*f* XPS spectra after electrochemical oxidation; b) quantitative analyses of IrO_x/Zr_2ON_2 and Ir black; and c) cyclic voltammetry curves normalized by the capacitive current of IrO_x/Zr_2ON_2.

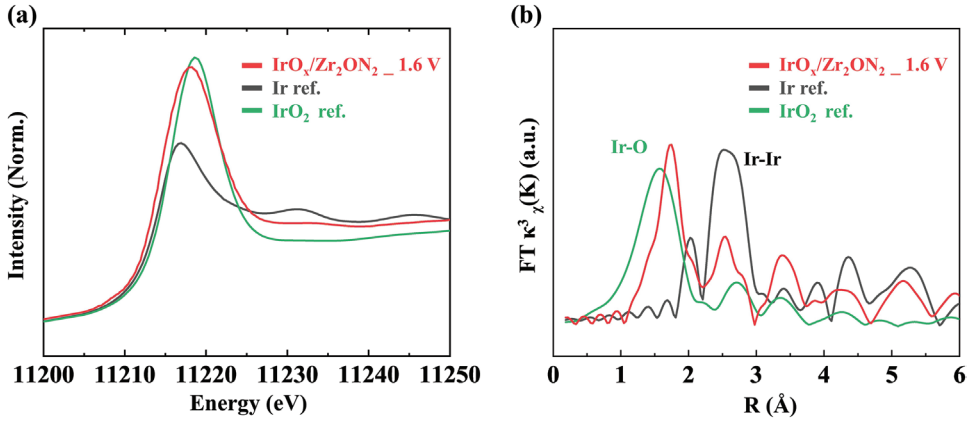

Figure 4. Chemical states and local atomic environments of the Ir species in IrO_x/Zr_2ON_2 under *operando* OER conditions at 1.6 V (vs RHE). a) Ir L_3-edge XANES spectra and b) Fourier transformed EXAFS (R-space with k-weight 3) analysis. Results are also shown for commercial metallic Ir NPs and IrO_2 NPs as references.

of Ir^{3+}/Ir^{4+} compared to commercial IrO_x. To clarify the stability of Zr_2ON_2 support materials, we analyzed Zr 3*d* XPS spectra (Figure S9a–c, Supporting Information) for IrO_x/Zr_2ON_2, IrO_x/ZrN, and IrO_x/ZrO_2 before and after the preliminary activation process. The deconvoluted Zr 3*d* peaks for all three samples showed no significant changes, indicating that the activation process exclusively affects on the supported IrO_x NPs. Furthermore, the deconvoluted O-Zr-N peaks of IrO_x/Zr_2ON_2 were maintained even after the 5 h stability test, as depicted in Figure S10 (Supporting Information). Likewise, the enhanced stability of IrO_x/Zr_2ON_2 compared to that of commercial IrO_x can be attributed to the relatively low Ir^{3+}/Ir^{4+} ratio and robustness of Zr_2ON_2 support material. From the XPS analysis, it can therefore be expected that the strong interaction between IrO_x and Zr_2ON_2 induces electron transfer from the support to the catalyst.

Additionally, the CV curves of electrochemically oxidized IrO_x/Zr_2ON_2 and IrO_x were measured, as shown in Figure 3c. It can be seen that prior to the OER, two redox couples were present. Subsequently, the A_1 and C_1 redox couple close to 0.9 V relates to the transition between Ir^{3+} and Ir^{4+}. At the same time, further oxidation beyond Ir^{4+} appears at a higher potential of 1.3 V,[32] and it can be clearly observed that the electrochemically oxidized IrO_x/Zr_2ON_2 showed a lower oxidation peak for A_1, thereby implying depletion of the Ir^{3+} chemical state, which is consistent with our XPS results. A similar shift of the Ir chemical oxidation states was also observed for IrO_x/ZrO_2 (Figures S7a,b and S11, Supporting Information), however, in this case, the relatively low electronic conductivity of ZrO_2 resulted in a significantly reduced OER activity. These results indicate the presence of a reduced chemical state with a lower Ir^{3+}/Ir^{4+} ratio for the IrO_x/Zr_2ON_2 electrocatalyst, which leads to an excellent stability in an acidic OER environment. Moreover, IrO_x/Zr_2ON_2 was found to exhibit a superior OER activity compared to IrO_x (Figure 2a,d,e), thereby implying that an additional activity-influencing factor must exist to compensate for the depletion of the highly active Ir^{3+} state.

Operando XAS measurements were carried out in an acidic OER environment using an applied voltage of 1.6 V to gain insight into the bulk oxidation state and local atomic environment of the electrochemically oxidized IrO_x/Zr_2ON_2 (denoted after IrO_x/Zr_2ON_2_1.6 V). As depicted in **Figure 4**a, the Ir L_3-edge X-ray absorption near edge structure (XANES) results for IrO_x/Zr_2ON_2_1.6 V and for the reference metallic Ir NPs and IrO_2 NPs show broad white lines related to transitions from the occupied 2p state to the empty 5d state.[33] More specifically, the peak position of this white line was 11218.09 eV for IrO_x/Zr_2ON_2_1.6 V, which is a slightly lower energy compared to that of the of commercial IrO_2 (i.e., 11218.69 eV), indicating the reduced chemical state of Ir. In addition, the oxidation state of Ir in the Ir/Zr_2ON_2_1.6 V electrode sample was calculated to be $Ir^{2.68+}$ based on the lever rule,[33,34] which is consistent with the reduced oxidation state of Ir determined by quantitative XPS analysis (i.e., $Ir^{2.92+}$). The corresponding Fourier transformed Ir L_3-edge extended X-ray absorption fine structure (EXAFS) results (R-space plot) of IrO_x/Zr_2ON_2_1.6 V in the acidic OER environment were then determined, as shown in Figure 4b. In this case, the peak at ≈1.56 Å in the reference IrO_2 corresponds to the Ir—O bond. However, interestingly, the Ir—O bond length in IrO_x/Zr_2ON_2_1.6 V (i.e., 1.72 Å) is longer than that of the reference IrO_2, implying the existence of tensile strain in the oxidized Ir catalyst. The oxidation state and coordination environment of the as-prepared IrO_x/Zr_2ON_2 were also investigated via ex situ XAS analysis, as depicted in Figure S12a,b (Supporting Information). Due to the fact that the reductive polyol process was employed to prepare the supported catalysts,[26b] the as-prepared IrO_x/Zr_2ON_2 possessed a lower Ir oxidation state (i.e., $Ir^{1.80+}$) than IrO_x/Zr_2ON_2_1.6 V, and clearly contains both Ir—O and Ir—Ir bonds. We further carried out a fitting of Fourier transformed Ir L_3-edge EXAFS data based on crystallographic information files (CIFs) for rutile IrO_2 and FCC Ir. Figure S13a–d (Supporting Information) showed the fitted Fourier transformed Ir L_3-edge EXAFS results for IrO_2 reference, Ir reference, as-prepared IrO_x/Zr_2ON_2, and IrO_x/Zr_2ON_2_1.6 V, respectively. Fitted parameters of EXAFS fitting were summarized in Table S4 (Supporting Information). In case of the IrO_2 and Ir references, the refined structural parameters (R-factor, interatomic distance change, and mean square relative displacement) exhibit only minor deviation from those predicted from each single CIFs. The Fourier transformed Ir

L_3-edge EXAFS spectra for as-prepared IrO_x/Zr_2ON_2 and IrO_x/Zr_2ON_2–1.6 V were successfully fitted with a combination of CIFs for the rutile IrO_2 and FCC Ir. The co-existance of Ir^{4+} and Ir^0 for IrO_x/Zr_2ON_2 even under the OER operating condition is identical result from the XPS analyses (Figure 3a,b; Figure S8a,b, Supporting Information). *Operando* XAS analyses further supported the presence of a reduced Ir oxidation state in IrO_x/Zr_2ON_2 compared to that of commercial IrO_2 in the acidic OER environment, and it was also confirmed that the tensile strain on the Ir—O bonds in IrO_x/Zr_2ON_2 enhanced the OER activity.

2.4. Theoretical Interpretation

To elucidate the origin of the enhanced catalytic activity of IrO_x/Zr_2ON_2, DFT calculations were performed using model systems for Ir and Ir supported on Zr_2ON_2 NPs. More specifically, the catalytic activities of these species in the OER were evaluated, and the reason behind the superior activity of the IrO_x NPs (IrO_x/Zr_2ON_2) compared to the isolated IrO_x NPs was considered, even though the former contained depleted Ir^{3+} oxidation states. For this purpose, a model structure of the Zr_2ON_2 NPs was built for the DFT calculations. This was achieved by generating hundreds of structures with random mixing of the O and N atom positions based on the space group of Zr_2ON_2 ($Ia\bar{2}$). The most stable configuration was selected for the simulated XRD in the atomic simulation environment (ASE) package[35] to compare the structural similarities between the experimental results and the simulation. As shown in Figure S14 (Supporting Information), the relative intensities and locations of the simulated XRD peaks are in good agreement with the experimental results, indicating that our slab model successfully represents the experiment.

The surface energies of the low-index surfaces, including the (100) and (111) surfaces, were then calculated, and it was found that the (111) surface possessed a significantly lower surface energy (0.048 eV $Å^{-2}$) than the (100) surface (0.311 eV $Å^{-2}$). Thus, a Zr_2ON_2 slab model was built based on the space group ($Ia\bar{2}$), an XRD comparison, and surface energy calculations. Due to the fact that the Ir NPs supported on Zr_2ON_2 exhibited (111) facets, and the Ir species itself possessed the lowest surface energy when the surface was terminated with (111) facets, the three Ir(111) layers were placed on top of the Zr_2ON_2(111) slab (Figure S15d, Supporting Information).

Electrochemical activity calculations were then carried out using surface Pourbaix diagrams with one monolayer (ML) of O*, OH*, and OOH* to consider the surface conditions under the applied OER potential. As shown in Figure S16 (Supporting Information), identical trends were observed with a small potential shift. More specifically, the O*-covered surface was favored at high potentials, OH* was stable in the medium potential range, and the bare Ir surface was stable at low potentials. Since the OER conditions employ a high potential range (i.e., >1.23 V), the fully oxidized surfaces were used to calculate the electrochemical OER activities of both the isolated IrO_x(111) and the IrO_x/Zr_2ON_2(111) surfaces. Thus, to construct a reaction energy diagram for the OER, the available intermediates and reaction steps were considered. More importantly, the theoretical OER activities were investigated using the adsorbate evolution mechanism (AEM) and the lattice oxygen-participating mechanism (LOM) (**Figure 5**c), Figure 5a,b shows the complete reaction energy diagrams following the LOM (red) or AEM (grey) mechanisms upon catalysis by IrO_x/Zr_2ON_2. As indicated, the isolated IrO_x NPs exhibited almost identical onset potentials (U_o = 2.04 V) for the LOM and the AEM due to the fact that the rate-determining step (RDS) is the formation of OH* from water (ΔG_1), which is independent of OOH* adsorption. However, a dramatic change in the catalytic activity was observed for IrO_x/Zr_2ON_2, wherein a significantly higher activity was found for the LOM (U_o = 1.56 V) compared to the AEM (U_o = 2.33 V), and the RDS changed to become the OOH* formation step ($\Delta G_{3\text{-}1}$). Thus, IrO_x/Zr_2ON_2 exhibited a lower onset potential (or higher activity) than the IrO_x surface. If the surface lattice oxygen is more favorable to change to OOH* by combining the adsorbed OH*, OER prefers to follow the LOM rather than the AEM.[36] Furthermore, several analyses were performed to identify the synergistic interactions between IrO_x and Zr_2ON_2. Initially, the lattice mismatch between Ir and Zr_2ON_2 generated an expansion of 4.4% in the supported IrO_x compared to that found in the original Ir surface (Figure 5d); this tensile strain decreased the OER performance of IrO_x owing to the presence of overly strong binding.[37] Additionally, it has been reported that structural distortion of Ir-based electrocatalysts, tuned by strain, surficial facet and defect, promotes OER activity with a faster filling of the oxygen vacancies in LOM process.[38] It should be noted here that according to our previous studies, the adsorbates on tensile-strained surfaces exhibit stronger binding energies than those on unstrained surfaces.[39]

The degree of charge transfer between IrO_x and the Zr_2ON_2 surface was then evaluated, and it was found that a total of 2.14 e^- were transferred from Zr_2ON_2 to the IrO_x surface as shown in Figure 5e. These donated electrons reduced IrO_x and activated the Ir—O bond, although the change in bond length was subtle (i.e., from 2.037 to 2.040 Å). According to our analyses, supported Ir should possess a stronger binding energy than isolated Ir, and as indicated by the binding energies presented in Table S5 (Supporting Information). Interestingly, the binding energy change for O* (0.857 eV) was significantly more extensive than those for OH* (0.482 eV) and OOH* (0.538 eV), and these differences originate from the different binding configurations. More specifically, O* usually prefers to bind at hollow sites, whereas OH* and OOH* bind at on-top or bridge sites. Thus, the binding energy of O* at the hollow sites is more significantly affected by the strain effect than those of OH* and OOH*. These differences changed the RDS from ΔG_1 to $\Delta G_{3\text{-}1}$. In other words, the energy difference between OOH* and O* became larger for IrO_x/Zr_2ON_2 than for IrO_x due to the fact that the sensitivity of the binding energy toward the strain is large for O* and small for OOH*; these results are consistent with previous literature reports.[37] As a result, the AEM pathway became less active because of the large $\Delta G_{3\text{-}1}$ energy, which in turn induces participation from the activated oxygen constituting the lattice Ir—O bonds (i.e., the LOM pathway) during the OER (red reaction pathway, Figure 5c). Moreover, based on the above DFT calculations, it was clear that $IrO_x/ZrON_2$ exhibits a lower theoretical onset potential (330 mV)

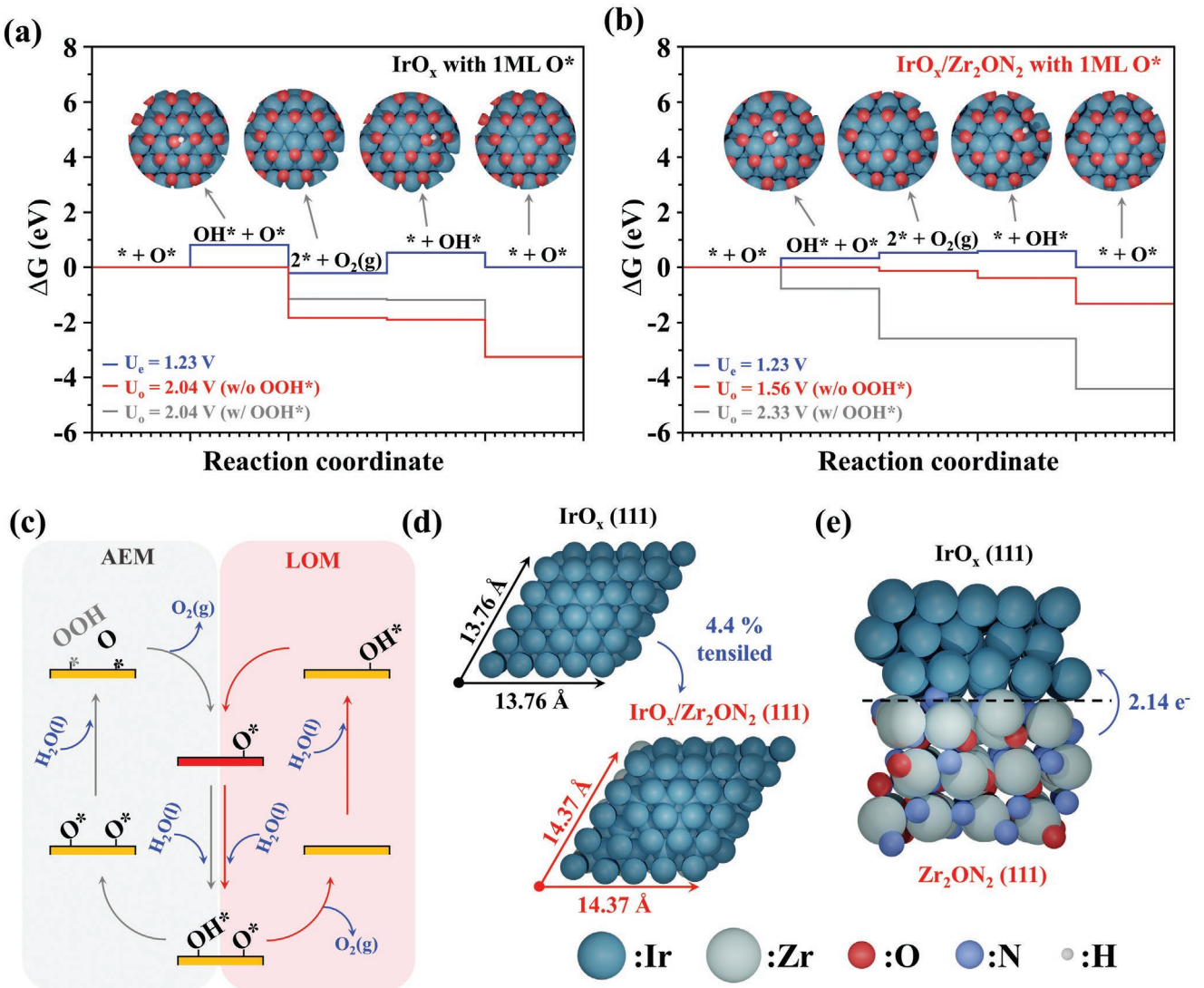

Figure 5. DFT-estimated reaction energy diagram for the OER on a) Ir with 1ML O* and b) on IrO_x/Zr_2ON_2 with 1 ML O*; c) schematic representations of the AEM (grey) and the LOM (red) for the OER; d) lattice comparison between IrO_x(111) and IrO_x/Zr_2ON_2(111); and e) charge transfer between IrO_x(111) and Zr_2ON_2(111).

than the isolated IrO_x NPs, which was therefore attributed to the altered reaction pathway from the conventional AEM to the LOM because of the tensile strain applied to the Ir—O bond and charge transfer from IrO_x to Zr_2ON_2.

3. Conclusion

IrO_x/Zr_2ON_2 electrocatalysts, which employ zirconium oxynitride (Zr_2ON_2) nanoparticles (NPs) as a support material, were prepared to break the trade-off between activity and stability in the oxygen evolution reaction (OER) of proton exchange membrane water electrolysis (PEMWE). More specifically, Zr_2ON_2 NPs (prepared via the sol–gel urea–glass route) were selected due to the fact that density functional theory (DFT) calculations showed that Zr_2ON_2 possesses a sufficient electrical conductivity (comparable to that of bulk graphite) and a superior thermodynamic stability than ZrN and ZrO_2. Thus, the desired IrO_x/Zr_2ON_2 electrocatalysts were obtained via a surfactant-free polyol method, followed by an electrochemical oxidation process. IrO_x/Zr_2ON_2 was found to exhibit a superior electrochemical performance compared to IrO_x/ZrN, IrO_x/ZrO_2, commercial IrO_x, and commercial IrO_x/TiO_2, with an overpotential of 255 mV at 10 mA cm^{-2} and a mass activity of 849 mA mg_{Ir}^{-1} at 1.55 V (vs the reversible hydrogen electrode). In addition, the electrochemical activity of IrO_x/Zr_2ON_2 was maintained with a negligible increase in voltage at a current density of 10 mA cm^{-2} for 5 h, while that of IrO_x/ZrN underwent severe degradation under the same conditions. This outstanding electrochemical performance was attributed to the strong interactions between IrO_x and the Zr_2ON_2 NPs (as verified by the adequate dispersion of IrO_x NPs without any segregation) and charge transfer from the support to the catalyst. Furthermore, *operando* X-ray absorption spectroscopy measurements under

an acidic OER environment indicated a reduced oxidation state of Ir and an extended Ir—O bond length for the IrO_x/Zr_2ON_2 electrocatalyst compared to an IrO_2 reference. Moreover, DFT calculations on isolated IrO_x NPs and IrO_x/Zr_2ON_2 with fully oxidized surfaces were conducted to provide insight into the experimental findings. A Zr_2ON_2 slab model was built based on the space group of la-3(206), the experimentally observed X-ray diffraction peaks, and surface energy calculations. It was found that IrO_x/Zr_2ON_2 exhibited a lower theoretical onset potential (330 mV) than the isolated IrO_x NP (790 mV) because the reaction pathway changed from a conventional adsorbate evolution mechanism to a lattice oxygen-participating mechanism due to tensile strain and charge transfer. Overall, these findings provide a novel strategy to overcome the trade-off relationship between the activity and stability for the acidic oxygen evolution of PEMWE.

4. Experimental Section

Chemicals: All chemicals were used as received without further purification. Zirconium(IV) chloride ($ZrCl_4$, >99.99% trace metal basis), hydrogen hexachloroiridate(IV) hydrate ($H_2IrCl_6{\cdot}xH_2O$, >99.9% trace metal basis), and urea (CON_2H_4, ≈99.0%) were purchased from Sigma-Aldrich. Ethanol (C_2H_6O, >99.9%), *n*-hexane (C_6H_{14}, >98.0%), ethylene glycol ($C_2H_6O_2$, >99.0%), and a 0.5 M aqueous sulfuric acid (H_2SO_4) solution were purchased from Daejung Chemical Company. Iridium power (Ir ≈325 mesh, ≈99.9% metal basis) and iridium(IV) oxide (IrO_2, ≈84.5% metal basis) were purchased from Alfa Aesar. The Nafion® 117 solution (≈5% in a mixture of lower aliphatic alcohols and water) was purchased from Sigma-Aldrich. Ultrapure deionized water (DI water, 18 MΩ cm^{-1}) was employed in all experiments.

Preparation of the Support Materials: To prepare the Zr-based support materials, a previously reported urea–glass route was employed, which is based on a sol–gel process.[25] Initially, zirconium chloride (1 g) was mixed with ethanol (2 g) and stirred for 30 min until a clear solution was obtained. Subsequently, urea (1 g) was slowly added to the alcoholic solution and the resulting solution was stirred for 30 min to completely dissolve the urea. After this time, the obtained solution was transferred to a quartz boat and dried at 70 °C for 30 min to form a zirconium–urea gel. To obtain the zirconium oxynitride (Zr_2ON_2) support, the zirconium–urea gel was heat-treated at 850 °C for 2 h under a 5% H_2 atmosphere (95% N_2). In contrast, to synthesize the zirconium nitride (ZrN) support, the zirconium–urea gel was heat-treated at 1000 °C for 24 h under an Ar atmosphere, and to obtain the zirconium oxide (ZrO_2) support, the zirconium–urea gel was heat-treated at 900 °C for 2 h under air. In each case, the resulting solid precipitates were collected and used without further washing.

Preparation of the Supported Iridium Nanoparticles: Different loadings of Ir NPs (i.e., 20, 40, and 60 wt.%) supported on the Zr_2ON_2, ZrN, and ZrO_2 supports were produced via the polyol method.[26] More specifically, the support material (40 mg) was mixed with ethylene glycol (20 mL) in a 50 mL vial and subjected to ultrasonication for 30 min. Subsequently, the appropriate volume of the Ir precursor solution ($H_2IrCl_6{\cdot}xH_2O$ in DI water, 100 mg mL^{-1}; 0.22, 0.59, or 1.33 mL, loadings of 20, 40, and 60 wt.%, respectively) was added to the resulting suspension and stirred for 30 min. The obtained mixtures were heat-treated at 170 °C for 3.5 h in an oil bath, and the resulting supported IrO_x NPs were washed three times with a hexane/ethanol mixture prior to collection by centrifugation. The IrO_x NPs were produced using a procedure similar to that used for the supported IrO_x NPs, but without the addition of the support materials.

Material Characterization: The morphologies, microstructures, elemental distributions, and compositions of the supported Ir electrocatalysts were analyzed using transmission electron microscopy (TEM) (Talos F200X, FEI, operated at 200 kW) and energy dispersive X-ray spectroscopy (EDS). The crystallinity of each electrocatalyst was observed using high-resolution X-ray diffractometry (HRXRD, SmartLab, RIGAKU) with Cu-Kα irradiation at 45 kV and 200 mA. The surface chemical states of the electrocatalysts were investigated using XPS (K-alpha, Thermo VG Scientific) with Al-Kα radiation (1486.6 eV). All energy data were calibrated according to the C 1s binding energy (284.8 eV) for the C–C components. The XAS spectra of the Ir L_3-edge (11215 eV) were collected at the 6D UNIST-PAL and BL8C beamlines of the Pohang Accelerator Laboratory (PAL) with a flux of 5×10^{12} photons s^{-1} at 300 mA and 2.5 GeV. In addition, X-ray absorption near-edge structure (XANES) and extended X-ray absorption fine structure (EXAFS) analyses were conducted using Athena and Artemis software (version 0.9.26).[40] A customized in situ cell was employed in the fluorescence mode to study the chemical states and coordination environments of the supported Ir electrocatalysts in an oxygen-evolving environment at 1.6 V (vs the reversible hydrogen electrode, RHE). For the *operando* XAS measurements, catalyst inks (50 mg catalyst, 10 µL 5% Nafion® 117 solution in 1 mL ethanol) were drop-casted onto carbon paper (active area: 1.5 × 1.5 cm^2). The counter and reference electrodes were a Pt wire and Hg/Hg_2SO_4 (in saturated K_2SO_4), respectively. The ex situ XAS spectra of commercial Ir and IrO_2 NPs were also collected for reference.

Electrochemical Measurements: The electrochemical properties of the supported Ir electrocatalysts were investigated using a conventional three-electrode electrochemical cell and a potentiostat (SP-50e, BioLogic). Pt wire and Hg/Hg_2SO_4 (in saturated K_2SO_4) were used as the counter and reference electrodes, respectively. A glassy carbon rotating disk electrode (5 mm diameter, geometrical area 0.196 cm^2; Pine Instruments) was used as the working electrode. All electrochemical measurements were carried out in Ar-saturated 0.5 M H_2SO_4. The applied potentials were referenced to the RHE using the standard calibration method ($E_{(RHE)} = E_{(Hg/Hg2SO4)} + 0.672$ V). The measured potentials were iR-corrected using high-frequency resistance (HFR) measured by electrochemical impedance spectroscopy (EIS). To prepare the working electrode, the catalyst (10 mg) was dispersed in a mixture of ethanol (1.0 mL) and a 5% Nafion® 117 solution (50 µL) under ultrasonication for 30 min. Subsequently, the catalyst ink (7.81 µL) was drop-cast onto a glassy carbon electrode to give a catalyst loading of 0.379 mg cm^{-2}. All catalysts were electrochemically oxidized by repeated cyclic voltammetry (CV) in the range of 0–1.50 V at a scan rate of 20 mV s^{-1} for five cycles prior to evaluating their electrocatalytic activities and stabilities toward the OER. The OER polarization curves were collected by sweeping the potential from 1.1 to 1.8 V at a scan rate of 2 mV s^{-1}. The overpotentials were calculated at a geometric current density of 10 mA cm^{-2}. The stability of each electrocatalyst was evaluated by chronopotentiometry for 5 h at 10 mA cm^{-2}. To determine the HFR and the charge transfer resistance (CTR), EIS was carried out at 1.53 V with an amplitude of 10 mV in the AC frequency range of 100 kHz to 0.1 Hz. To investigate single cell performances of IrO_x/Zr_2ON_2, membrane electrode assembly (MEA) was fabricated with conventional Decal transfer method. IrO_x/Zr_2ON_2, Pt/C (TEC10E50E, Tanaka) and Nafion®115 were used as anode electrocatalyst, cathode electrocatalyst, and polymer electrolyte membrane, respectively. The transferred loading amount for the anode and cathode were 0.4 mg_{Ir} cm^{-2} and 0.32 mg_{Pt} cm^{-2}, respectively. A commercial MEA (anode: 2.0 mg_{Ir} cm^{-2}, cathode: 0.5 mg_{Pt} cm^{-2}, Nafion®115, Hiat gGmbH) was used for comparison.

Computational Details: GGA-level spin-polarized DFT calculations were performed with the Vienna ab initio simulation package using a plane-wave basis set with a cutoff energy of 400 eV. The Perdew–Burke–Ernzerhof functional[41] was used to describe the electron exchange and correlation. The DFT+U method was employed to treat the localized Zr 4d orbitals with an effective U value of 4.0 eV.[42] The Brillouin zone was sampled with a 2 × 2 × 1 k-point mesh following the Monkhorst–Pack scheme. The convergence criteria for the electronic and geometry optimizations were 10^{-5} eV and 10^{-2} eV $Å^{-1}$, respectively. Two different structures were constructed, one consisting of a monometallic Ir(111) surface with two frozen bottom layers and two top relaxed layers (Figure S15a,b, Supporting Information), and the other consisting of

Ir(111) surfaces supported a $Zr_2ON_2(111)$ surface (Figure S15c,d, Supporting Information). Both the Ir(111) and $Zr_2ON_2(111)$ surfaces were three layers thick, wherein the bottom two layers of $Zr_2ON_2(111)$ were fixed in their bulk positions. All systems were constructed using a 20 Å vacuum gap in the *z*-direction to avoid self-interaction. To calculate the electrochemical OER activities of the surface systems, the following reaction steps were considered with and without the presence of an OOH* adsorbate:[43]

$$\Delta G_1 : H_2O(l) + * \leftrightarrow OH^* + \left(H^+ + e^-\right) \quad (1)$$

$$\Delta G_2 : OH^* \leftrightarrow O^* + \left(H^+ + e^-\right) \quad (2)$$

$$\Delta G_{3-1} : O^* + H_2O(l) \leftrightarrow OOH^* + \left(H^+ + e^-\right) \quad (3)$$

$$\Delta G_{4-1} : OOH^* \leftrightarrow O_2(g) + * + \left(H^+ + e^-\right) \quad (4)$$

$$\Delta G_{3-2} : O^* + * + H_2O(l) \leftrightarrow O^* + OH^* + \left(H^+ + e^-\right) \quad (5)$$

$$\Delta G_{4-2} : O^* + OH^* \leftrightarrow O_2(g) + 2* + \left(H^+ + e^-\right) \quad (6)$$

The OER overpotential (η) was calculated using a reaction energy diagram drawn according to the following equations:[44]

$$\Delta G(U) = \Delta E + \Delta ZPE - T\Delta S + neU \quad (7)$$

$$\eta = U_o - 1.23\,V \quad (8)$$

where ΔE is the reaction energy, ΔZPE is the zero-point energy correction, ΔS is the entropy change, U is the applied potential, and U_o is the onset potential for the OER. The chemical potential of the solvated proton and electron pair ($H^+ + e^-$) at standard conditions ($p_{H_2} = 1$ bar, $a_{H^+} = 1$, T = 298.15 K) was calculated as 0.5 $\mu^0_{H_2(g)} - eU$ by assuming equilibrium at the standard hydrogen electrode.[45]

Supporting Information

Supporting Information is available from the Wiley Online Library or from the author.

Acknowledgements

C.L., K.S., and Y.P. contributed equally to this work. This work was supported by the framework of Research and Development Program of the Korea Institute of Energy Research (KIER) (C3-2420) and a Commercialization Promotion Agency for R&D Outcomes (COMPA) grant funded by the Korean government (MSIT) (No. 2021E100). It was supported by the Korea Institute of Energy Technology Evaluation and Planning (KETEP) and the Ministry of Trade, Industry & Energy (MOTIE) of the Republic of Korea (No. 20218520040040). H.Y.K. acknowledges the financial support from a National Research Foundation of Korea (NRF) grant funded by the Basic Science Research Program through the NRF funded by the Ministry of Education (No. 2021R1A6A1A03043682). DFT calculations were supported by the Welch Foundation (F-1841) and the Extreme Science and Engineering Discovery Environment (XSEDE) program through the allocation TG-CHE190010 from the Texas Advanced Computing Center (TACC). The XAS experiments at PAL-II 6D UNIST-PAL and 8C beamlines were supported in part by MIST, Pohang University of Science and Technology (POSTECH), and Ulsan National Institute of Science & Technology (UNIST) Central Research Facilities.

Conflict of Interest

The authors declare no conflict of interest.

Data Availability Statement

The data that support the findings of this study are available from the corresponding author upon reasonable request.

Keywords

electrocatalysts, iridium, oxygen evolution reaction, proton exchange membrane water electrolysis, support materials

Received: February 10, 2023
Published online: March 17, 2023

[1] J. R. Ortenero, A. E. S. Choi, M. A. B. Promentilla, *Chem. Eng. Trans.* **2022**, *94*, 1141.
[2] A. Weiß, A. Siebel, M. Bernt, T.-H. Shen, V. Tileli, H. Gasteiger, *J. Electrochem. Soc.* **2019**, *166*, F487.
[3] S. S. Kumar, V. Himabindu, *Mater. Sci. Energy Technol.* **2019**, *2*, 442.
[4] M. Bernt, A. Hartig-Weiß, M. F. Tovini, H. A. El-Sayed, C. Schramm, J. Schröter, C. Gebauer, H. A. Gasteiger, *Chem. Ing. Tech.* **2020**, *92*, 31.
[5] C. Lee, K. Shin, C. Jung, P.-P. Choi, G. Henkelman, H. M. Lee, *ACS Catal.* **2019**, *10*, 562.
[6] L. She, G. Zhao, T. Ma, J. Chen, W. Sun, H. Pan, *Adv. Funct. Mater.* **2022**, *32*, 2108465.
[7] A. Badgett, M. Ruth, B. James, B. Pivovar, *Curr. Opin. Chem. Eng.* **2021**, *33*, 100714.
[8] C. Minke, M. Suermann, B. Bensmann, R. Hanke-Rauschenbach, *Int. J. Hydrogen Energy* **2021**, *46*, 23581.
[9] S. M. Alia, S. Stariha, R. L. Borup, *J. Electrochem. Soc.* **2019**, *166*, F1164.
[10] C. Daiane Ferreira da Silva, F. Claudel, V. Martin, R. Chattot, S. Abbou, K. Kumar, I. Jiménez-Morales, S. Cavaliere, D. Jones, J. Rozière, L. Solà-Hernandez, C. Beauger, M. Faustini, J. Peron, B. Gilles, T. Encinas, L. Piccolo, F. H. B. de Lima, L. Dubau, F. Maillard, *ACS Catal.* **2021**, *11*, 4107.
[11] a) J. Chen, P. Cui, G. Zhao, K. Rui, M. Lao, Y. Chen, X. Zheng, Y. Jiang, H. Pan, S. X. Dou, W. Sun, *Angew. Chem., Int. Ed.* **2019**, *58*, 12540; b) C. Spöri, P. Briois, H. N. Nong, T. Reier, A. Billard, S. Kühl, D. Teschner, P. Strasser, *ACS Catal.* **2019**, *9*, 6653; c) A. Hartig-Weiss, M. Miller, H. Beyer, A. Schmitt, A. Siebel, A. T. Freiberg, H. A. Gasteiger, H. A. El-Sayed, *ACS Appl. Nano Mater.* **2020**, *3*, 2185; d) J. Xu, Z. Lian, B. Wei, Y. Li, O. Bondarchuk, N. Zhang, Z. Yu, A. Araujo, I. Amorim, Z. Wang, B. Li, L. Liu, *ACS Catal.* **2020**, *10*, 3571.
[12] S. Abbou, R. Chattot, V. Martin, F. Claudel, L. Solà-Hernández, C. Beauger, L. Dubau, F. Maillard, *ACS Catal.* **2020**, *10*, 7283.
[13] a) M. Bernicke, D. Bernsmeier, B. Paul, R. Schmack, A. Bergmann, P. Strasser, E. Ortel, R. Kraehnert, *J. Catal.* **2019**, *376*, 209; b) J. Cheng, J. Yang, S. Kitano, G. Juhasz, M. Higashi, M. Sadakiyo, K. Kato, S. Yoshioka, T. Sugiyama, M. Yamauchi, N. Nakashima, *ACS Catal.* **2019**, *9*, 6974; c) E. Oakton, D. Lebedev, M. Povia, D. F. Abbott, E. Fabbri, A. Fedorov, M. Nachtegaal, C. Copéret, T. J. Schmidt, *ACS Catal.* **2017**, *7*, 2346.
[14] B. Liu, S. Wang, C.-Y. Wang, B.-Z. Ma, Y.-Q. Chen, *Int. J. Miner., Metall. Mater.* **2020**, *27*, 264.

[15] Z. Shi, J. Li, J. Jiang, Y. Wang, X. Wang, Y. Li, L. Yang, Y. Chu, J. Bai, J. Yang, *Angew. Chem., Int. Ed.* **2022**, *61*, e202212341.
[16] a) Z. Shi, Y. Wang, J. Li, X. Wang, Y. Wang, Y. Li, W. Xu, Z. Jiang, C. Liu, W. Xing, J. Ge, *Joule* **2021**, *5*, 2164; b) Z. Wang, W. Gao, Q. Xu, X. Ren, S. Xu, S. Zhu, X. Niu, X. Li, R. Zhao, Y. Han, G. Li, Q. Wang, *ChemElectroChem* **2021**, *8*, 418.
[17] Y. Zhao, J. Hu, C.-L. Chiang, Y. Li, W. Yang, Z. Yang, W.-H. Hung, Y.-G. Lin, Z. Chen, B. Li, P. Gao, H. Li, *J. Mater. Chem. A* **2022**, *10*, 20964.
[18] a) G. Li, K. Li, L. Yang, J. Chang, R. Ma, Z. Wu, J. Ge, C. Liu, W. Xing, *ACS Appl. Mater. Interfaces* **2018**, *10*, 38117; b) K. Zhang, W. Mai, J. Li, H. Wang, G. Li, W. Hu, *J. Mater. Sci.* **2020**, *55*, 3507.
[19] a) Y. Zhong, X. Xia, F. Shi, J. Zhan, J. Tu, H. J. Fan, *Adv. Sci.* **2016**, *3*, 1500286; b) L. Ma, S. Sui, Y. Zhai, *J. Power Sources* **2008**, *177*, 470.
[20] Y. C. Kimmel, X. Xu, W. Yu, X. Yang, J. G. Chen, *ACS Catal.* **2014**, *4*, 1558.
[21] S. Clarke, C. Michie, M. Rosseinsky, *J. Solid State Chem.* **1999**, *146*, 399.
[22] X.-Z. Wang, T. P. Muneshwar, H.-Q. Fan, K. Cadien, J.-L. Luo, *J. Power Sources* **2018**, *397*, 32.
[23] M. Laurikaitis, S. Burinskas, J. Dudonis, D. Milčius, *J. Phys.: Conf. Ser.* **2008**, *100*, 082051.
[24] M. Carmo, D. L. Fritz, J. Mergel, D. Stolten, *Int. J. Hydrogen Energy* **2013**, *38*, 4901.
[25] a) C. Giordano, C. Erpen, W. Yao, B. Milke, M. Antonietti, *Chem. Mater.* **2009**, *21*, 5136; b) C. Giordano, M. Antonietti, *Nano Today* **2011**, *6*, 366.
[26] a) F. Bonet, V. Delmas, S. Grugeon, R. H. Urbina, P. Silvert, K. Tekaia-Elhsissen, *Nanostruct. Mater.* **1999**, *11*, 1277; b) F. Fiévet, S. Ammar-Merah, R. Brayner, F. Chau, M. Giraud, F. Mammeri, J. Peron, J.-Y. Piquemal, L. Sicard, G. Viau, *Chem. Soc. Rev.* **2018**, *47*, 5187.
[27] Y. Zhao, M. Luo, S. Chu, M. Peng, B. Liu, Q. Wu, P. Liu, F. M. de Groot, Y. Tan, *Nano Energy* **2019**, *59*, 146.
[28] Y. Yuan, J. Wang, S. Adimi, H. Shen, T. Thomas, R. Ma, J. P. Attfield, M. Yang, *Nat. Mater.* **2020**, *19*, 282.
[29] A. Lončar, D. Escalera-López, S. Cherevko, N. Hodnik, *Angew. Chem., Int. Ed.* **2022**, *61*, 202114437.
[30] S. Cherevko, S. Geiger, O. Kasian, A. Mingers, K. J. Mayrhofer, *J. Electroanal. Chem.* **2016**, *774*, 102.
[31] a) O. Kasian, S. Geiger, T. Li, J.-P. Grote, K. Schweinar, S. Zhang, C. Scheu, D. Raabe, S. Cherevko, B. Gault, K. J. Mayrhofer, *Energy Environ. Sci.* **2019**, *12*, 3548; b) O. Kasian, J. P. Grote, S. Geiger, S. Cherevko, K. J. Mayrhofer, *Angew. Chem., Int. Ed.* **2018**, *57*, 2488.
[32] a) J. F. Rivera, I. Pignot-Paintrand, E. Pereira, B. L. Rivas, J.-C. Moutet, *Electrochim. Acta* **2013**, *110*, 465; b) K. E. Michaux, R. W. Murray, *Langmuir* **2013**, *29*, 12254; c) R. Kötz, in *Spectroscopic and Diffraction Techniques in Interfacial Electrochemistry* (Eds: C. Gutiérrez, C. Melendres), Springer, Dordrecht **1990**, p. 409.
[33] H. N. Nong, T. Reier, H.-S. Oh, M. Gliech, P. Paciok, T. H. T. Vu, D. Teschner, M. Heggen, V. Petkov, R. Schlögl, T. Jones, P. Strasser, *Nat. Catal.* **2018**, *1*, 841.
[34] S. C. Purdy, P. Ghanekar, G. Mitchell, A. J. Kropf, D. Y. Zemlyanov, Y. Ren, F. Ribeiro, W. N. Delgass, J. Greeley, J. T. Miller, *ACS Appl. Energy Mater.* **2020**, *3*, 1410.
[35] a) T. Iwasa, K. Nobusada, *J. Phys. Chem. C* **2007**, *111*, 45; b) D. Waasmaier, A. Kirfel, *Acta Cryst.* **1995**, *51*, 416.
[36] L. Yang, K. Zhang, H. Chen, L. Shi, X. Liang, X. Wang, Y. Liu, Q. Feng, M. Liu, X. Zou, *J. Energy Chem.* **2022**, *66*, 619.
[37] a) W. Sun, Z. Wang, W. Q. Zaman, Z. Zhou, L. Cao, X.-Q. Gong, J. Yang, *Chem. Commun.* **2018**, *54*, 996; b) W. Sun, Z. Zhou, W. Q. Zaman, L.-m. Cao, J. Yang, *ACS Appl. Mater. Interfaces* **2017**, *9*, 41855.
[38] F. Wang, C. Zhang, H. Yang, *J. Energy Chem.* **2022**, *70*, 623.
[39] Y. Park, K. Shin, C. Lee, S.-Y. Lee, Y.-K. Lee, C.-H. Kim, H.-S. Cho, G. Henkelman, H. M. Lee, *Chem. Eng. J.* **2022**, *446*, 136966.
[40] B. Ravel, M. Newville, *J. Synchrotron Rad.* **2005**, *12*, 537.
[41] a) J. P. Perdew, K. Burke, M. Ernzerhof, *Phys. Rev. Lett.* **1996**, *77*, 3865; b) Y. Zhang, W. Yang, *Phys. Rev. Lett.* **1998**, *80*, 890.
[42] L. Wang, T. Maxisch, G. Ceder, *Phys. Rev. B* **2006**, *73*, 195107.
[43] I. C. Man, H. Y. Su, F. Calle-Vallejo, H. A. Hansen, J. I. Martínez, N. G. Inoglu, J. Kitchin, T. F. Jaramillo, J. K. Nørskov, J. Rossmeisl, *ChemCatChem* **2011**, *3*, 1159.
[44] a) J. Rossmeisl, G. S. Karlberg, T. Jaramillo, J. K. Nørskov, *Faraday Discuss.* **2009**, *140*, 337; b) J. K. Nørskov, J. Rossmeisl, A. Logadottir, L. Lindqvist, J. R. Kitchin, T. Bligaard, H. Jonsson, *J. Phys. Chem. B* **2004**, *108*, 17886; c) S. Liu, M. G. White, P. Liu, *J. Phys. Chem. C* **2016**, *120*, 15288.
[45] A. A. Peterson, F. Abild-Pedersen, F. Studt, J. Rossmeisl, J. K. Nørskov, *Energy Environ. Sci.* **2010**, *3*, 1311.